

Time domain potential and source methods and their application to twin-hull high speed crafts

KARA, Fuat

Available from Sheffield Hallam University Research Archive (SHURA) at:

<https://shura.shu.ac.uk/29602/>

This document is the Published Version [VoR]

Citation:

KARA, Fuat (2022). Time domain potential and source methods and their application to twin-hull high speed crafts. Ships and Offshore Structures. [Article]

Copyright and re-use policy

See <http://shura.shu.ac.uk/information.html>



Time domain potential and source methods and their application to twin-hull high-speed crafts

Fuat Kara

To cite this article: Fuat Kara (2022): Time domain potential and source methods and their application to twin-hull high-speed crafts, Ships and Offshore Structures, DOI: [10.1080/17445302.2022.2035560](https://doi.org/10.1080/17445302.2022.2035560)

To link to this article: <https://doi.org/10.1080/17445302.2022.2035560>



© 2022 The Author(s). Published by Informa UK Limited, trading as Taylor & Francis Group



Published online: 20 Feb 2022.



Submit your article to this journal [↗](#)



Article views: 97



View related articles [↗](#)



View Crossmark data [↗](#)

Time domain potential and source methods and their application to twin-hull high-speed crafts

Fuat Kara

Engineering & Mathematics, Sheffield Hallam University, Sheffield, UK

ABSTRACT

The numerical accuracy of time dependent potential and source methods is compared against analytical and other numerical results using an in-house transient wave-body interaction three-dimensional wave Green function computational tool of ITU-WAVE. The time dependent Impulse Response Functions (IRFs) are used to predict the behaviour of radiation forces, exciting forces, and response of floating bodies. For radiation force IRFs, the numerical results show that potential method converges with less numbers of panels compared to source method, while in the case of diffraction force IRFs, the convergence is achieved with the same number of elements for both potential and source methods. As potential method achieves convergence faster than source method for radiation force IRFs prediction, potential method is applied for the hydrodynamic and response parameters of a twin-hull high-speed craft. The present ITU-WAVE numerical results, which are compared with experimental, analytical, and other numerical results for validation purposes show satisfactory agreements.

ARTICLE HISTORY

Received 8 August 2021
Accepted 13 January 2022

KEYWORDS

Boundary integral equation method; potential and source methods; seakeeping; single- and multi-hull bodies; with and without forward speed; transient wave Green function

Nomenclature

a_{jk}	frequency independent added-mass at infinity
b_{jk}	frequency independent damping coefficients
c_{jk}	frequency independent restoring coefficients
A_{jk}	frequency dependent added-mass coefficients
B_{jk}	frequency dependent damping coefficients
F_{jk}	radiation forces
F_{jD}	diffraction forces
g	gravitational acceleration
G	transient free surface Green function
J_0	zero order Bessel function
k	wave number
K_{jS}	scattering impulse response functions
K_{jI}	incident wave impulse response functions
K_{jk}	radiation impulse response functions
L, B, T	length, breadth, draft
l - n - s	tangential -normal y -direction local coordinate system
n_j	normal vector in j -th direction
n_1	normal vector in x -direction
N	total panel number
m_j	gradient of steady velocity in j -th direction
\hat{p}	transient pressure
$P(x, y, z)$	field point
$Q(\xi, \eta, \varsigma)$	source point
r	distance between field and source points
r'	distance between field and image points
R	distance between field and source points on the free surface
S_0	body surface at mean position
S_b	body surface for boundary surface of the floating system
S_∞	surface at infinity for boundary surface of the floating system
t	time
t_N	current time step
U_0	constant body velocity in the x -direction
\vec{V}	disturbance fluid velocity
X_j	complex form of diffraction forces
β	time dependent phase of generated waves and heading angle
Δt	constant time step size
ζ	incident wave elevation
λ	wavelength
μ	relative position of field and source points
ϖ	position of the floating system in the wave direction on the free surface

ρ	seawater density
σ	source strength
Γ	intersection between the instantaneous body surface and free surface
φ	transient potential
φ_I	transient incident wave potential
ϕ_S	transient scattering wave potential
Φ	total disturbance velocity potential
χ_k	transient potential in k -th mode
ψ_{1k}	instantaneous fluid response to body motion
ψ_{2k}	potential due to steady translation
ω	absolute frequency
ω_c	critical frequency
ω_e	encounter frequency

1. Introduction

The fluid-body interaction with and without forward speed effects of the three-dimensional single- or multi-hull floating systems cause unsteady motions due to ambient incident wave environment and requires the prediction of global and local responses of the floating systems at sea. The global and local responses are the functions of the hydrodynamic parameters which are due to the disturbances by incident waves and can be predicted with the three-dimensional linear or nonlinear methods. The solution of Navier-Stokes equations results in complete and accurate predictions of the hydrodynamic parameters (Zou et al. 2019). Alternatively, the fluid flow behaviour at the near field could be modelled with Navier-Stokes equations to consider the viscous effects which are dominant near to floating bodies while the potential predictions can be used at the far field as viscous effects decrease. As it is important to have computationally efficient methods for routine calculations, the viscous related methods are still computationally intensive for practical purposes.

The frequency and time domain potential methods can be used for the prediction of the hydrodynamic parameters to avoid computationally expensive viscous approximations. A two-dimensional potential strip theory, which ignores the viscous effects, is

developed and used in industry and academia successfully (Korvin-Kroukovsky and Jacobs 1957; Ogilvie and Tuck 1969; Salvensen et al. 1970; Kim et al. 1980). As the potential strip theory methods predict the hydrodynamic parameters accurately and are very efficient computationally, they find a wide range of applications in industry for conventional ships and floating systems. However, the strip theory methods have shortcomings for complex geometries at the range of low frequency and high forward speed.

The frequency and time domain three-dimensional methods, which uses panels to define the geometries, can be used to avoid the shortcomings of the strip theory methods, in which the interactions between strips are ignored. In the case of the three-dimensional methods, the influence of panels on each other are automatically considered. Although there are many types of three-dimensional methods, two popular methods, which are wave Green function and Rankine panel method in both frequency and time domains, are used to take the three-dimensional effects into account. The wave Green function methods (Liapis and Beck 1985; Liapis 1986; King 1987; Lin and Yue 1990; Kara 2000; Inoue and Kamruzzaman 2008) satisfy the condition at infinity and free surface boundary condition automatically, which result in the only discretisation of the body surface to satisfy the boundary condition. However, in the case of Rankine panel methods (Nakos and Sclavounos 1990; Kring and Sclavounos 1991; Xiang and Faltinsen 2011; Yuan et al. 2014), the condition at infinity and body boundary condition is satisfied by the discretisation of both body surface and some part of the free surface, which result in additional computational load. In the context of linear analysis, the frequency and time domain parameters depend on each other through Fourier transform.

The semi nonlinear methods in which the coupling of steady and unsteady problems is satisfied automatically at the forward speed (Ferrant 1990; Beck and Magee 1991; Danmeier 1999) can be used to predict nonlinear motions of the floating systems. One of the semi nonlinear numerical methods is the *body exact* method in which the free surface boundary condition is satisfied with transient wave Green function implying that the free surface boundary condition is linearised while the body boundary condition is satisfied instantaneously – implying that nonlinear effects of the time varying of the body motion is considered exactly. As the body boundary condition is satisfied instantaneously, the responses of the floating systems are not sinusoidal anymore. This implicitly means that the frequency and time domain results do not depend on each other through Fourier transform in the *body exact* method. The free surface effect is presented with convolution integral which requires the recalculation of transient wave Green function up to the present time. This makes the *body exact* method computationally expensive.

The mixed Euler–Lagrange method, which has Lagrangian and Eulerian steps, is used to predict the fully nonlinear behaviour of the floating systems (Longuet-Higgins and Cokelet 1976; Faltinsen 1977; Vinje and Brevig 1981; Baker et al. 1982; Beck 1999; Kara et al. 2007). The linear boundary value problem is solved with the Eulerian step for the integration of free surface boundary condition using the fluid velocities, while the Lagrangian step is used to integrate the nonlinear free surface boundary condition in time. The superiority of the time domain methods over the frequency domain methods, which can be only applied to linear systems, is that the nonlinear and transient effects can be easily included with the linear and nonlinear time domain methods. The time dependent and nonlinear problems that can be solved with the time domain methods include the transient effects on floating systems’ hydroelasticity, prediction of nonlinear hydrostatic coefficients, nonlinear roll damping with semi-empirical methods, transient behaviour of the first order steady forces, nonlinear effects on cable forces, manoeuvring under

unsteady motions, motion of floating systems with large amplitudes, water on deck, and forward speed with variable speeds.

The present study is original, and its novel part is the application of the present method on the high-speed crafts and getting very satisfactory agreement with experimental results. In this respect, the present study addresses the shortcomings and fills the gap on high-speed crafts with very high Froude number $F_n = 0.75$ and contributes to knowledge in this field. To the best of the author’s knowledge, the present transient wave Green function method was not studied and applied before, to predict the hydrodynamic parameters of the high-speed crafts with a very high Froude number $F_n = 0.75$.

The Time dependent Boundary Integral Equation Method (BIEM) is used to describe the fluid boundaries while the Green theorem is applied over the transient wave Green function. In addition, basis flow is selected as the free stream which results in Neumann-Kelvin linearisation of the exact initial boundary value problem (Kara 2000, 2007, 2010, 2011, 2015, 2016a, 2016b, 2016c, 2017, 2020a, 2020b, 2012a, 2021b, 2021c). The radiation and exciting convolution integrals are solved with the trapezoidal rule while the potentials over the discretised quadrilateral elements are considered constant. The linear algebraic equation for the solutions of the source strengths and potentials in time is obtained by satisfying the body boundary condition at the collocation points of each quadrilateral element in the in-house computational tool ITU-WAVE. The experimental and analytical results are used to validate the accuracy of predicted hydrodynamic parameters of the ITU-WAVE numerical results.

2. Boundary integral equation of source and potential methods

The potential theory approximations assume that the fluid is incompressible, inviscid, and has irrotational flow implying no lifting effect and fluid separation from the free surface. Laplace equation $\nabla^2\Phi(P, t) = 0$ controls the fluid domain while the fluid velocities $\vec{V}(P, t) = \nabla\Phi(P, t)$ are determined with the gradient of the harmonic velocity potential $\Phi(P, t)$. The transient integral equations with potential method Equation (1) (Kara 2000) whose memory effect is presented with transient wave Green function is used to describe the initial value problem (Wehausen and Laitone 1960). The initial value problem in the absence of a body is satisfied by the transient wave Green function (Finkelstein 1957).

$$\begin{aligned} \varphi(P, t) + \frac{1}{2\pi} \iint_{S_{b(t)}} dS_Q \varphi(Q, t) \frac{\partial}{\partial n_Q} \left(\frac{1}{r} - \frac{1}{r'} \right) \\ = \frac{1}{2\pi} \iint_{S_{b(t)}} dS_Q \left(\frac{1}{r} - \frac{1}{r'} \right) \frac{\partial}{\partial n_Q} \varphi(Q, t) - \frac{1}{2\pi} \int_{t_0}^t d\tau \iint_{S_{b(\tau)}} dS_Q \\ \left\{ \varphi(Q, \tau) \frac{\partial}{\partial n_Q} \tilde{G}(P, Q, t - \tau) - \tilde{G}(P, Q, t - \tau) \frac{\partial}{\partial n_Q} \varphi(Q, \tau) \right\} \\ - \frac{U_0^2}{2\pi g} \int_{t_0}^t d\tau \oint_{\Gamma(\tau)} d\eta \left\{ \varphi(Q, \tau) \frac{\partial}{\partial \xi} \tilde{G}(P, Q, t - \tau) - \tilde{G}(P, Q, t - \tau) \frac{\partial}{\partial \xi} \varphi(Q, \tau) \right\} \\ + \frac{U_0}{2\pi g} \int_{t_0}^t d\tau \oint_{\Gamma(\tau)} d\eta \left\{ \varphi(Q, \tau) \frac{\partial}{\partial \tau} \tilde{G}(P, Q, t - \tau) - \tilde{G}(P, Q, t - \tau) \frac{\partial}{\partial \tau} \varphi(Q, \tau) \right\} \end{aligned} \quad (1)$$

On the other hand, the source method is preferred to predict the fluid velocities around the floating systems since they can be easily

obtained as the gradient of the velocity potential in Equation (3), while the spatial derivatives of the velocity potential in Equation (1) – which include additional complexity to the solution – is required in the case of the potential method. The time dependent source strength $\sigma(P, t)$, which represents the flow behaviour around the floating system, is given in integral equation form in Equation (2).

$$\begin{aligned} \frac{1}{2}\sigma(P, t) + \frac{1}{4\pi} \iint_{S_{b(t)}} dS_Q \frac{\partial}{\partial n_P} \left(\frac{1}{r} - \frac{1}{r'} \right) \sigma(Q, t) = -\frac{\partial}{\partial n_P} \varphi(P, t) \\ - \frac{1}{4\pi} \int_{t_0}^t d\tau \iint_{S_{b(\tau)}} dS_Q \frac{\partial}{\partial n_P} \tilde{G}(P, Q, t - \tau) \sigma(Q, \tau) \\ - \frac{U_0^2}{4\pi g} \int_{t_0}^t d\tau \oint_{\Gamma(\tau)} d\eta n_1 \frac{\partial}{\partial n_P} \tilde{G}(P, Q, t - \tau) \sigma(Q, \tau) \end{aligned} \quad (2)$$

and velocity potential around floating systems is presented in Equation (3)

$$\begin{aligned} \varphi(P, t) = -\frac{1}{4\pi} \iint_{S_{b(t)}} dS_Q \left(\frac{1}{r} - \frac{1}{r'} \right) \sigma(Q, t) \\ - \frac{1}{4\pi} \int_{t_0}^t d\tau \iint_{S_{b(\tau)}} dS_Q \tilde{G}(P, Q, t - \tau) \sigma(Q, \tau) \\ - \frac{U_0^2}{4\pi g} \int_{t_0}^t d\tau \oint_{\Gamma(\tau)} d\eta n_1 \tilde{G}(P, Q, t - \tau) \sigma(Q, \tau) \end{aligned} \quad (3)$$

where

$$\begin{aligned} \tilde{G}(P, Q, t, \tau) = 2 \int_0^\infty dk \sqrt{kg} \sin(\sqrt{kg}(t - \tau)) e^{k(z+s)} J_0(kR) \\ R = \sqrt{(x - \xi + U_0 t)^2 + (y - \eta)^2} \\ r = \sqrt{(x - \xi)^2 + (y - \eta)^2 + (z - s)^2} \\ r' = \sqrt{(x - \xi)^2 + (y - \eta)^2 + (z + s)^2} \end{aligned} \quad (4)$$

where the intersection between the free surface and floating body is given with $\Gamma(t)$, while the memory part of the transient wave Green function is given with $\tilde{G}(P, Q, t, \tau)$. The field and source points in time are presented with $P(x(t), y(t), z(t))$ and $Q(\xi(t), \eta(t), s(t))$ respectively. The separation distances between the source and field points as well as the field and image points about xy -plane or $z = 0$ are given with r and r' , respectively, while the zero order Bessel function is represented with J_0 . The impulsive disturbance at time τ at the integration point $Q(\xi(t), \eta(t), s(t))$ results in the velocity potential at time t at the field point $P(x(t), y(t), z(t))$ which is represented with the memory part of the transient wave Green function $\tilde{G}(P, Q, t, \tau)$.

The time dependent potential $\varphi(P, t)$ in the potential method is obtained directly by the solution of the time dependent boundary integral equation, Equation (1). In the case of the indirect or source method, the time dependent source strength $\sigma(P, t)$ in Equation (2) is first solved. It is then used to predict the potential $\varphi(P, t)$ in

Equation (3) and the gradient of potential $\nabla\varphi(P, t)$, which result in the fluid velocities around the floating system. The time marching scheme is used to solve the integral equation for potential in Equation (1) for the potential method as well as the source strength in Equation (2), potential and gradient of the potential in Equation (3) for the source method. The same integral equation may be used for radiation and scattering potentials as the only difference is the body boundary conditions, which are the inputs on the right-hand side of Equations (1) and (2). Only body surface under mean position needs to be discretised with panels as the condition at infinity and free surface boundary conditions are automatically satisfied with the transient wave Green function. The discretisation of the body surface results in the replacement of a finite number of unknown source strength in Equation (2) or potential in Equation (1) with the continuous singularity distribution. The linear algebraic equation for the solution of potential and source strengths over each panel is then obtained by satisfying the integral equations in Equations (1) and (2), respectively, at null points of each panel at which induced velocities are zero.

Hess and Smith (1964) method is used for the analytical integration of $1/r$ and $1/r'$ in Equations (1–3) over each panel. Exact integration, multipole expansion and monopole expansion are used for the small, intermediate and large values of r and r' , respectively. The memory part of the transient wave Green function $\tilde{G}(P, Q, t, \tau)$ in Equation (4) is predicted analytically (Liapis 1986; King 1987; Kara 2000), while its integration over each panel is done numerically with 2×2 Gaussian quadrature after mapping the panels into unit squares. The integration on line elements is done with 16 Gaussian points, after subdividing interaction elements into straight lines. It is assumed that the line elements' potential or source strength equals to those of the panels underneath them.

$\tilde{G}(P, Q, t - \tau) = \sqrt{g/r'^3} \tilde{G}(\mu, \beta)$ is used to present the memory part of the transient wave Green function while the nondimensional form $\tilde{G}(\mu, \beta) = 2 \int_0^\infty d\lambda \sqrt{\lambda} \sin(\beta\sqrt{\lambda}) e^{-\lambda\mu} J_0(\lambda\sqrt{1-\mu^2})$ is the function of two nondimensional parameters of $\mu = -(z + s)/r'$ which varies from zero to one and represents the vertical coordinate, $\beta = \sqrt{g/r'}(t - \tau)$ which is the time dependent phase of generated waves, nondimensional $\lambda = kr'$ which is related to the field and source points of relative positions. The prediction of the transient wave Green function $\tilde{G}(P, Q, t - \tau)$ requires computationally efficient numerical methods depending on nondimensional (μ, β) parameters to reduce computational time. As only one solution is not suited for the prediction due to the convergence problem, five different analytical methods are used including asymptotic expansion of the complex error function, Bessel function, Filon quadrature, asymptotic expansion and power series expansion.

3. Comparison of time dependent potential and source methods

3.1. Radiation force impulse response functions (IRFs)

The time dependent radiation forces $F_{jk}(t)$ due to the motion in the k -th and j -th directions are given as (Cummins 1962).

$$F_{jk}(t) = -a_{jk}\ddot{x}_k(t) - b_{jk}\dot{x}_k(t) - c_{jk}x_k(t) - \int_0^t d\tau K_{jk}(t - \tau)\dot{x}_k(\tau) \quad (5)$$

where

$$a_{jk} = \rho \iint_{S_0} dS_Q \psi_{1k}(Q) n_j \quad (6)$$

$$b_{jk} = \rho \iint_{S_0} dS_Q (\psi_{1k}(Q) m_j - \psi_{2k}(Q) n_j) \quad (7)$$

$$c_{jk} = -\rho \iint_{S_0} dS_Q \psi_{2k}(Q) m_j \quad (8)$$

$$K_{jk}(t) = \rho \iint_{S_0} dS_Q \left\{ \frac{\partial}{\partial t} \chi_k(Q, t) n_j - \chi_k(Q, t) m_j \right\} \quad (9)$$

The time dependent accelerations, velocities and displacements of the floating system in mean position S_0 are given with $\ddot{x}_k(t)$, $\dot{x}_k(t)$, $x_k(t)$, respectively, while the integration points and field points are represented with Q, P , respectively. The unit normal vector and the coupling of steady and unsteady potential at each direction are presented with n_j , $m_j = (0, 0, 0, 0, U_0 n_3, -U_0 n_2)$, respectively. The transient radiation force in Equation (5) is the function of the displacement, velocity, acceleration ($x_k(t)$, $\dot{x}_k(t)$, $\ddot{x}_k(t)$), convolution integral representing the damping effects of the free surface, and time independent hydrodynamic coefficients (a_{jk} , b_{jk} , c_{jk}). The frequency and time independent acceleration, velocity, and displacement coefficients are given by a_{jk} related to added-mass coefficient depending on geometry, b_{jk} related to damping coefficient and c_{jk} related to hydrostatic restoring coefficient depending on forward speed and geometry, respectively. The impulsive velocity potential is used to predict the time dependent hydrodynamic parameters. The IRFs $K_{jk}(t)$, which depend on time, forward speed and geometry in j -th and k -th directions, are used to represent the memory effect of the free surface after an initial disturbance of the free surface at zero time. The velocity potentials for the instantaneous fluid response to the disturbances and steady velocity in Equation (6) and Equation (7) are represented with $\psi_{1k}(P)$ and $\psi_{2k}(P)$, respectively, while the time dependent transient velocity potential in Equation (9) is given with $\chi_k(P, t)$ (Ogilvie 1964).

3.1.1. Zero-speed case with potential and source methods

In the context of potential theory, the hydrodynamic parameters may be predicted with either the direct (potential) or the source (indirect) method (Kara 2000). The fluid velocities on the floating systems can be directly obtained with source formulation while

the predictions of the fluid velocities with the potential method are not straight forward as the gradient of the potential in space is required. The present numerical results with both direct and indirect methods of the in-house transient ITU-WAVE computational tool, which uses the transient wave Green function for the approximations of hydrodynamic parameters, are used to predict heave IRF. The predicted IRFs from potential and source methods with the ITU-WAVE numerical tool are compared against each other and analytically defined heave IRF of a hemisphere with radius R . The analytically defined heave IRF is obtained with inverse Fourier transform of the frequency domain added-mass or damping coefficients (Hulme 1982).

The convergence test with respect to panel numbers is presented in Figure 1(a) for hemisphere heave IRF with the potential method at Froude number $Fn = 0.0$. It can be seen in Figure 1(a) that the present ITU-WAVE numerical results perfectly predict the analytical heave IRF (Hulme 1982) when the panel numbers are increased with nondimensional time step $\Delta t \sqrt{g/R} = 0.05$. The potential method with time domain approximations is used for the prediction of IRFs by other researchers including Adachi and Ohmatsu (1979), Newman (1985), Beck and Liapis (1987).

The present in-house ITU-WAVE numerical result for the hemisphere with panel number 400 and nondimensional time step size 0.05 at Froude number $Fn = 0.0$ is compared with the analytical result (Hulme 1982) in Figure 1(b). It can be observed in Figure 1(b) that present numerical and analytical results are matched very well even at longer times.

The convergence test using the source or indirect method for the hemisphere with a nondimensional time step 0.05 and in a range of panel numbers are presented at Froude number $Fn = 0.0$ in Figure 2(a). When the potential method in Figure 1(a) and the source method in Figure 2(a) using the same number of panels for numerical prediction are compared, the source method shows oscillations at longer times. However, as can be observed in Figure 2(b), the oscillations at longer times are decreased when the panel numbers in the source method are increased – which implies that computational time would increase considerably, if the same accuracy from both direct and indirect methods is required.

The potential method with panel number 400 and the source method with panel number 1444 are used to compare the present ITU-WAVE computational results with analytical heave IRF (Hulme 1982) in Figure 3(a). Although the same level of accuracy could be achieved with both direct and indirect methods, the source method requires considerably higher panel numbers.

The numerical results of the potential and source methods with a small number of panels $pn = 36$ are compared with analytical

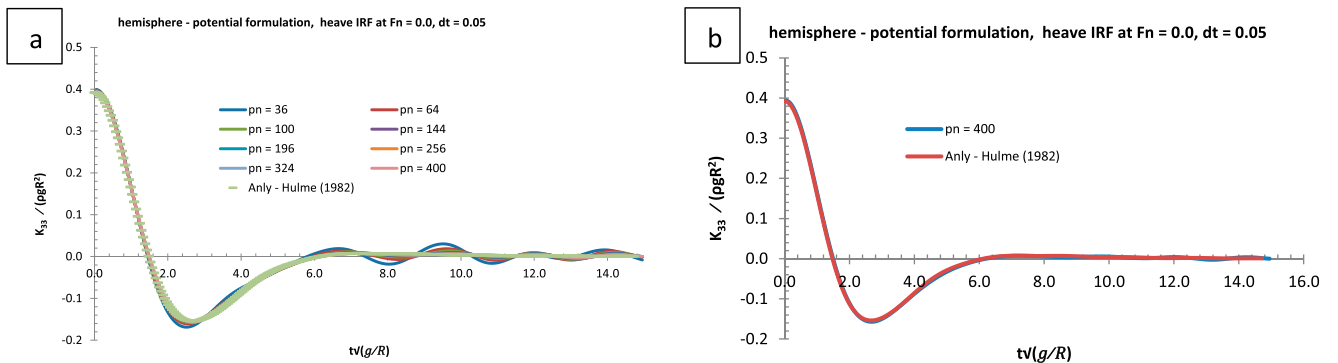


Figure 1. Potential method, radiation heave IRF of a hemisphere with radius R – convergence test in a range of panel numbers with a nondimensional time step size 0.05 at Froude number $Fn = 0.0$. (This figure is available in colour online.)

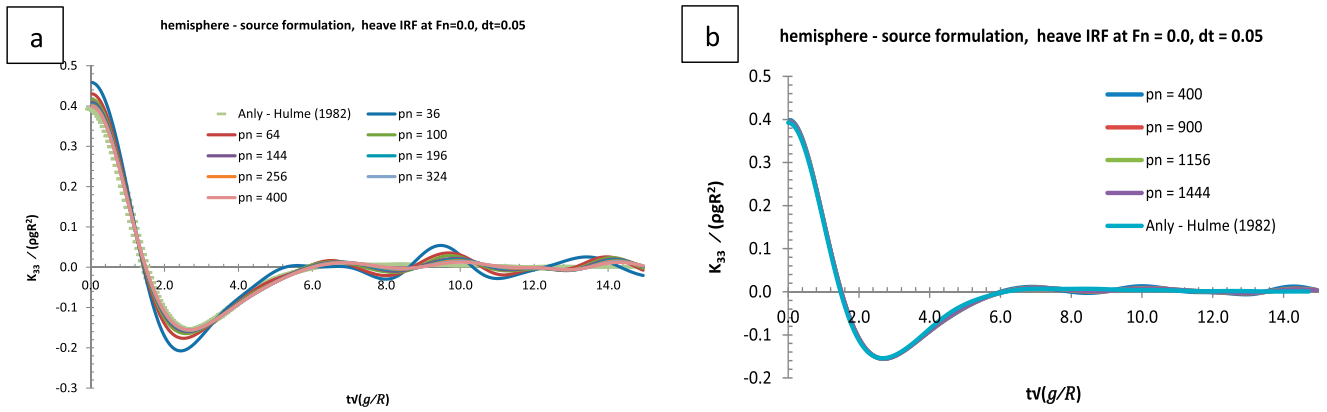


Figure 2. Source method, radiation heave IRF of a hemisphere with radius R – convergence test in a range of panel numbers with a nondimensional time step size 0.05 at Froude number $F_n = 0.0$. (This figure is available in colour online.)

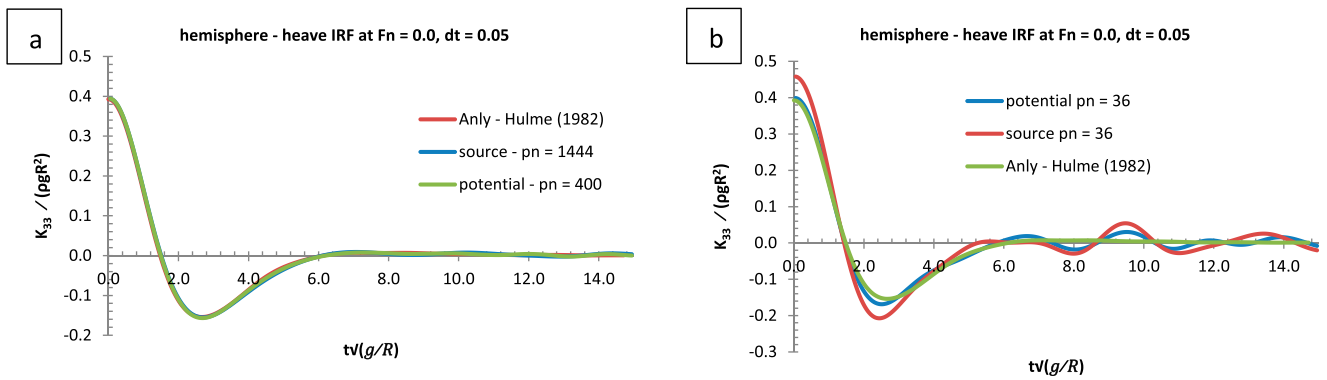


Figure 3. Comparison of radiation heave IRFs for a hemisphere with radius R at Froude number $F_n = 0.0$ and nondimensional time step size 0.05. (This figure is available in colour online.)

heave IRF (Hulme 1982) in Figure 3(b). It may be noticed in Figure 3(a) that even with a small panel number, the potential method approximates the analytical result in an acceptable level while it is not the case for the source method, which shows the discrepancies at lower times and the larger oscillations at longer times.

3.1.2. Forward-speed case with potential and source methods

As the line integral exists in the case of the forward speed, a modified Wigley hull form (Journee 1992) for both potential and source methods are used at Froude number $F_n = 0.3$ for the convergence test to determine the effects of line integral which is

considered in the next Section 3.1.2.1. The modified Wigley hull form has parabolic sections and has the length to beam ratio $L/B = 10$ and length to draft ratio $L/T = 16$. The modified Wigley hull form is defined analytically in Equation (10).

$$\eta = (1 - \varsigma^2)(1 - \xi^2)(1 + 0.2\xi^2) + \varsigma^2(1 - \varsigma^8)(1 - \xi^2)^4 \quad (10)$$

where $\eta = 2y/B$, $\xi = 2x/L$, and $\varsigma = z/T$. The draft, beam, and length are given with T , B , and L , respectively. Figure 4 shows heave and pitch IRFs with potential formulation at a range of

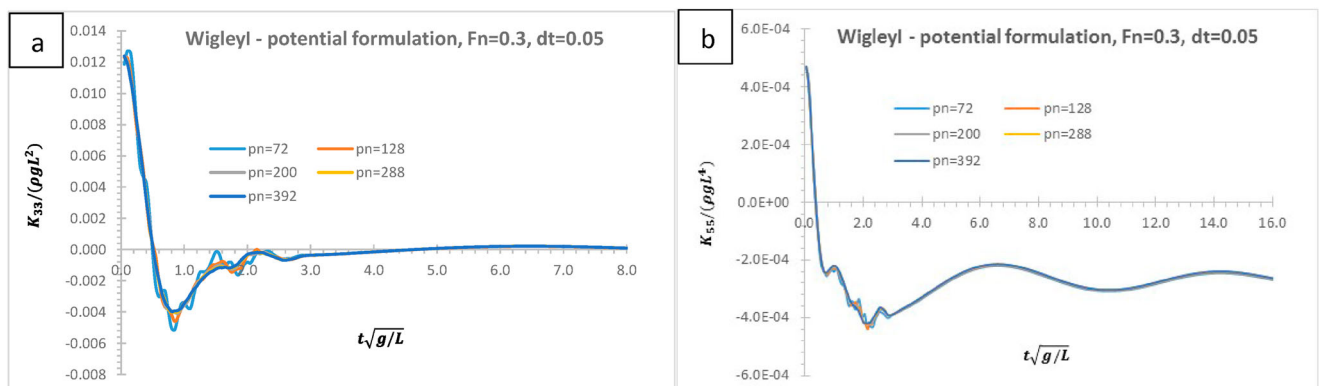


Figure 4. Potential method for Wigley hull form with Froude number $F_n = 0.3$, nondimensional time step size $dt = 0.05$, in a range of increasing panel numbers (a) heave IRF (b) pitch IRF. (This figure is available in colour online.)

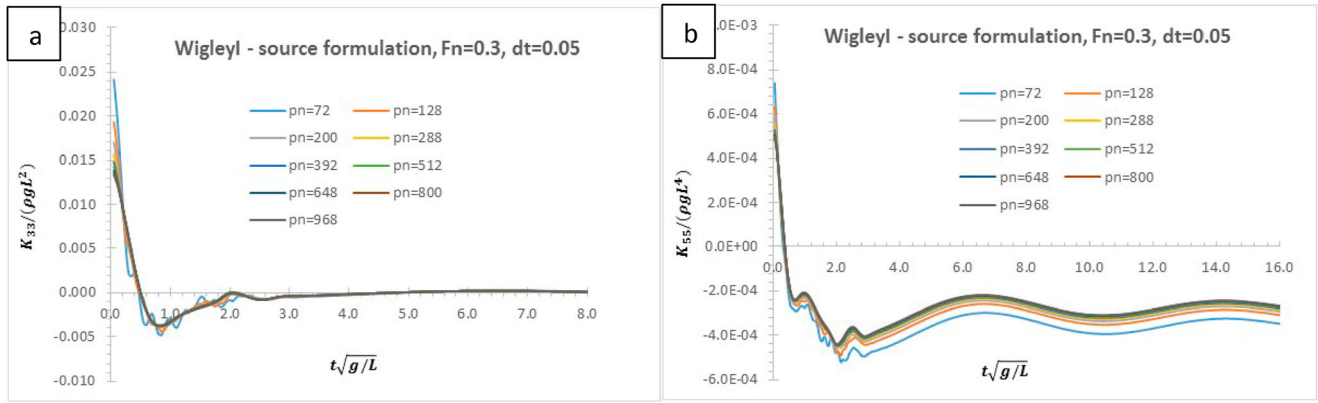


Figure 5. Source method for Wigley hull form with Froude number $F_n = 0.3$, nondimensional time step size $dt = 0.05$, in a range of increasing panel numbers (a) heave IRF (b) pitch IRF. (This figure is available in colour online.)

increasing panel numbers. It can be observed from Figure 4 that IRFs are converged with even small panel number, $pn = 288$.

Figure 5 shows heave and pitch IRFs with source formulation at a range of increasing panel numbers. It can be observed from Figure 5 that IRFs with source approximation require more panels for convergence compared to the potential formulation. Besides, in the case of source formulation, the pitch IRF at longer times is converged more slowly compared to the potential method.

When potential and source formulations are compared for both zero and forward speed cases, a potential approach gives better accurate results with a small number of elements. The same accuracy can be achieved with source formulation if the number of panels is increased.

3.1.2.1. Line integral effect in potential and source methods. As mentioned in the previous section, in the case of the forward speed, line integrals of the potential formulation in Equation (1) exists and the solutions of $\frac{\partial}{\partial \xi} \varphi(Q, \tau)$ and $\frac{\partial}{\partial \tau} \varphi(Q, \tau)$ in Equation (11) are not easily predicted.

$$\begin{aligned}
 & -\frac{U_0^2}{2\pi g} \int_{t_0}^t d\tau \oint_{\Gamma(\tau)} d\eta \left\{ \varphi(Q, \tau) \frac{\partial}{\partial \xi} \tilde{G}(P, Q, t - \tau) - \tilde{G}(P, Q, t - \tau) \frac{\partial}{\partial \xi} \varphi(Q, \tau) \right\} \\
 & + \frac{U_0}{2\pi g} \int_{t_0}^t d\tau \oint_{\Gamma(\tau)} d\eta \left\{ \varphi(Q, \tau) \frac{\partial}{\partial \tau} \tilde{G}(P, Q, t - \tau) - \tilde{G}(P, Q, t - \tau) \frac{\partial}{\partial \tau} \varphi(Q, \tau) \right\}
 \end{aligned} \quad (11)$$

It can be shown (Liapis 1986) that the unknown term $\frac{\partial}{\partial \xi} \varphi(Q, \tau)$ in the first term of Equation (11) can be approximated in the l-n-s (tangential -normal y-direction) local coordinate system for wall-sided bodies at waterline using the properties of the integration by parts

$$\begin{aligned}
 & \oint_{\Gamma(\tau)} d\eta \tilde{G}(P, Q, t - \tau) \frac{\partial}{\partial \xi} \varphi(Q, \tau) \cong \oint_{\Gamma(\tau)} d\eta \tilde{G}(P, Q, t - \tau) \frac{\partial}{\partial n} \varphi(Q, \tau) (\vec{n} \cdot i) \\
 & + \oint_{\Gamma(\tau)} d\eta \tilde{G}(P, Q, t - \tau) \frac{\partial}{\partial s} \varphi(Q, \tau) (\vec{s} \cdot i) \\
 & \times \oint_{\Gamma(\tau)} d\eta \varphi(Q, \tau) \frac{\partial}{\partial l} \tilde{G}(P, Q, t - \tau) (\vec{l} \cdot i) \\
 & \times \oint_{\Gamma(\tau)} dl \varphi(Q, \tau) \tilde{G}(P, Q, t - \tau) \frac{\partial}{\partial l} (\vec{l} \cdot i) (\vec{l} \cdot j)
 \end{aligned} \quad (12)$$

As the term $(\vec{s} \cdot i)$ equals zero for wall-sided bodies, the second term in the right-hand side of Equation (12) is considered zero as most of the interested bodies are wall-sided at the waterline. The x- and y-velocity components are used to predict the l-tangential derivative of the Green function in Equation (13)

$$\frac{\partial}{\partial l} \tilde{G}(P, Q, t - \tau) = n_2 \frac{\partial}{\partial \xi} \tilde{G}(P, Q, t - \tau) + n_1 \frac{\partial}{\partial \eta} \tilde{G}(P, Q, t - \tau) \quad (13)$$

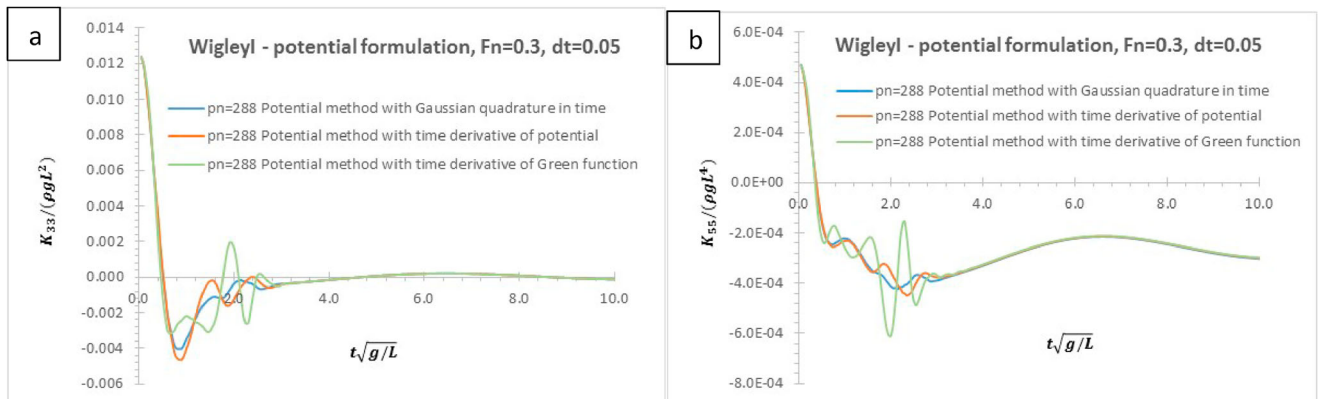


Figure 6. potential formulation, (a) heave IRF, (b) pitch IRFs for Wigley hull form with $F_n = 0.3$, $dt = 0.05$. (This figure is available in colour online.)

The prediction of the line integrals, which result from the application of potential formulation Stoke's theorem on the free surface, is done by subdividing the waterline to the straight line depending on the number of sections that are used on the free surface. The potential or source strength of the waterline segments is equal to those of the panels just below them at the $z = 0$ plane.

The time derivative of the potential $\frac{\partial}{\partial \tau} \varphi(Q, \tau)$ in the second term of Equation (11) is integrated by parts to get Equation (14) using boundary condition over the Green function and potential which equals zero at time $t = 0$.

$$\begin{aligned} & \frac{U_0}{2\pi g} \int_{t_0}^t d\tau \oint_{\Gamma(\tau)} d\eta \left\{ \varphi(Q, \tau) \frac{\partial}{\partial \tau} \tilde{G}(P, Q, t - \tau) - \tilde{G}(P, Q, t - \tau) \frac{\partial}{\partial \tau} \varphi(Q, \tau) \right\} \\ &= \frac{U_0}{\pi g} \int_{t_0}^t d\tau \oint_{\Gamma(\tau)} d\eta \varphi(Q, \tau) \frac{\partial}{\partial \tau} \tilde{G}(P, Q, t - \tau) \end{aligned} \quad (14)$$

Alternatively, the time derivative of the Green function $\frac{\partial}{\partial \tau} \tilde{G}(P, Q, t - \tau)$ in the second term of Equation (11) is integrated by parts to get Equation (15) with respect to the potential.

$$\begin{aligned} & \frac{U_0}{2\pi g} \int_{t_0}^t d\tau \oint_{\Gamma(\tau)} d\eta \left\{ \varphi(Q, \tau) \frac{\partial}{\partial \tau} \tilde{G}(P, Q, t - \tau) - \tilde{G}(P, Q, t - \tau) \frac{\partial}{\partial \tau} \varphi(Q, \tau) \right\} \\ &= \frac{U_0}{\pi g} \int_{t_0}^t d\tau \oint_{\Gamma(\tau)} d\eta \tilde{G}(P, Q, t - \tau) \frac{\partial}{\partial \tau} \varphi(Q, \tau) \end{aligned} \quad (15)$$

The numerical experience has shown that the time derivative of the Green function $\frac{\partial}{\partial \tau} \tilde{G}(P, Q, t - \tau)$ gets larger near time $t = 0$ and generates larger oscillation as shown in Figure 6 although the analytical prediction of $\frac{\partial}{\partial \tau} \tilde{G}(P, Q, t - \tau)$ is known in time. It is also shown by the numerical experience in Figure 6 that as the potential in time varies slowly, Equation (15) gives a better approximation compared to Equation (14). However, it was also found through numerical experience that Equation (15) does not give expected accurate numerical results when the trapezoidal integration is used mainly due to the oscillatory nature and amplitude of the time domain Green function $\tilde{G}(P, Q, t - \tau)$ near the free surface when $(t - \tau)$ becomes smaller.

As it is presented in Figure 6, the line integral in Equation (15) can be predicted more accurately using Gaussian Quadrature in time and assuming that potential over each panel is constant and

can be approximated as

$$\begin{aligned} & \frac{U_0}{\pi g} \int_{t_0}^{t_N} d\tau \oint_{\Gamma(\tau)} d\eta \tilde{G}(P, Q, t - \tau) \frac{\partial}{\partial \tau} \varphi(Q, \tau) = \frac{1}{\Delta t} \sum_{n=1}^{N-1} [\varphi(Q, t_{n+1}) \\ & - \varphi(Q, t_n)] \oint_{\Gamma(\tau)} d\eta \int_{t_n}^{t_{n+1}} d\tau \tilde{G}(P, Q, t - \tau) \end{aligned} \quad (16)$$

In the case of the source formulation, line integrals are involved with a normal derivative of the Green function in Equation (2) and the Green function itself in Equation (3). When compared to the potential formulation, it is easier to predict the line integrals with source approximation, as the predictions do not require additional simplifications of the potential or time domain Green function. However, the source formulation requires more panel numbers to converge as it is presented in Figure 7.

It may be noticed in Figure 7 that potential approximation requires $pn = 288$ panel numbers, while it is panel number $pn = 800$, in the case of source formulation.

3.1.2.2. Asymptotic continuation. One of the important differences between with and without forward speed cases is the decay characteristics of the transient wave Green function and IRFs. In the case of the with forward speed, the time domain transient wave Green function, and hence, the IRFs oscillate at the critical reduced frequency $\tau = \omega_c U_0/g = 1/4$ which cause resonance and slow decay of the functions in time. The wave system around the floating bodies at critical reduced frequency $\tau = \omega_c U_0/g = 1/4$ results in the generation of the energy. In the case of the without forward speed, this energy propagates away from the body while it stays at the vicinity of the floating system as the wave components' group velocity is approximately the same as with floating body speed in the case of the with forward speed. This physical behaviour can be explained by the asymptotic continuation of the leading order contribution of the time domain Green function (Newman 1992).

$$\tilde{G}(P, Q, t - \tau) \cong \frac{\sqrt{2}}{U^2 t} e^{\left(\frac{z}{4U^2}\right)} \sin(\omega_c t) \quad (17)$$

As the time and frequency domain results are linked to each other via Fourier transform, the frequency domain Green function (Dagan and Miloh 1980) results can be obtained by the Fourier transform of Equation (17). The asymptotic continuation in Equation (17) also shows that the time dependent Green function at a forward speed oscillates at the critical reduced frequency with a decay rate of $1/t$. As the solution of the integral equation

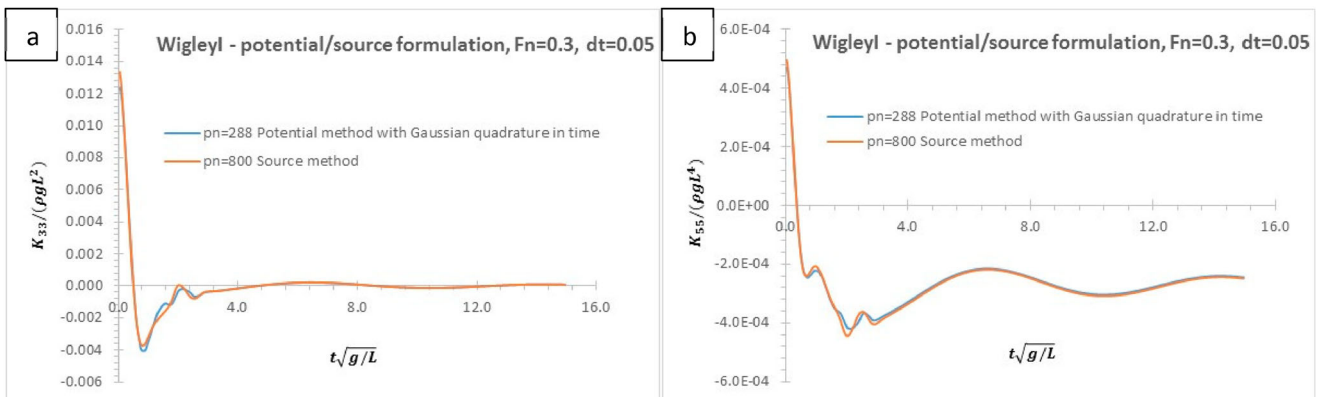


Figure 7. Potential and source formulation comparison, (a) heave IRF, (b) pitch IRFs for Wigley hull form with $F_n = 0.3$, $dt = 0.05$. (This figure is available in colour online.)

is dictated by the transient wave Green function, similar decays are expected for the boundary integral equation and IRFs.

The $\tau = 1/4$ resonance at a critical reduced frequency $\tau = \omega_c U_0/g = 1/4$ causes the time domain IRFs solution to decay slowly and results in the large time asymptotic behaviour of the transient problem. When the forward speed and zero forward speed cases are compared, transients take more time to decay in the case of the forward speed. As the decay of the IRFs at the forward speed takes significantly large computational time, an asymptotic continuation is proposed Bingham (1994) to reduce the expensive computational time. As shown in Equation (17), the decay rate of the IRFs is proportional to $1/t$ and can be approximated as

$$K_{jk}(t) \cong a_0 + \frac{1}{t}[a_1 \cos(\omega_c t) + a_2 \sin(\omega_c t)] \quad (18)$$

The least squares fit is used to determine the constants a_0 , a_1 and a_2 in Equation (18), after truncating the computation of the IRFs at a non-dimensional time step of $15\sqrt{g/L}$. This asymptotic continuation also supports that the time domain linearised approximation at the critical reduced frequency $\tau = \omega_c U_0/g = 1/4$ has a finite solution. The long ITU-WAVE numerical calculation and asymptotic continuation of heave IRFs are compared in Figure 8. As can be observed from Figure 8, which include the expanded view of the long simulation with ITU-WAVE and asymptotic continuation, both results are matched very well. This comparison shows that the simulation of the motion of floating systems can be extended to any length without requiring the computationally expensive

numerical prediction of the transient wave Green function at each time step for a very long simulation.

The effect of the critical reduced frequency on frequency dependent added-mass and damping coefficients for Wigley hull form at Froude number $F_n = 0.3$ can be clearly observed in Figure 9, which include experimental results of Journee (1992) for comparison purpose, at around non-dimensional absolute frequency $\omega\sqrt{L/g} \cong 0.838$.

3.2. Diffraction (Froude-Krylov and scattering) force IRFs

The time dependent diffraction forces $F_{jD}(t)$ in j -th direction, which are the superposition of scattering and Froude-Krylov forces, are the functions of IRFs and incident waves and may be written as (King 1987).

$$F_{jD}(t) = \int_{-\infty}^{\infty} d\tau K_{jD}(t-\tau)\zeta(\tau) = \int_{-\infty}^{\infty} d\tau \{K_{jS}(t-\tau) + K_{jI}(t-\tau)\}\zeta(\tau) \quad (19)$$

$$K_{jI}(t) = \iint_{S_0} dS_Q \hat{p}(Q, t)n_j \quad (20)$$

$$K_{jS}(t) = \rho \iint_{S_0} dS_Q \left\{ -\frac{\partial}{\partial t} \hat{\phi}_S(Q, t)n_j + \hat{\phi}_S(Q, t)m_j \right\} \quad (21)$$

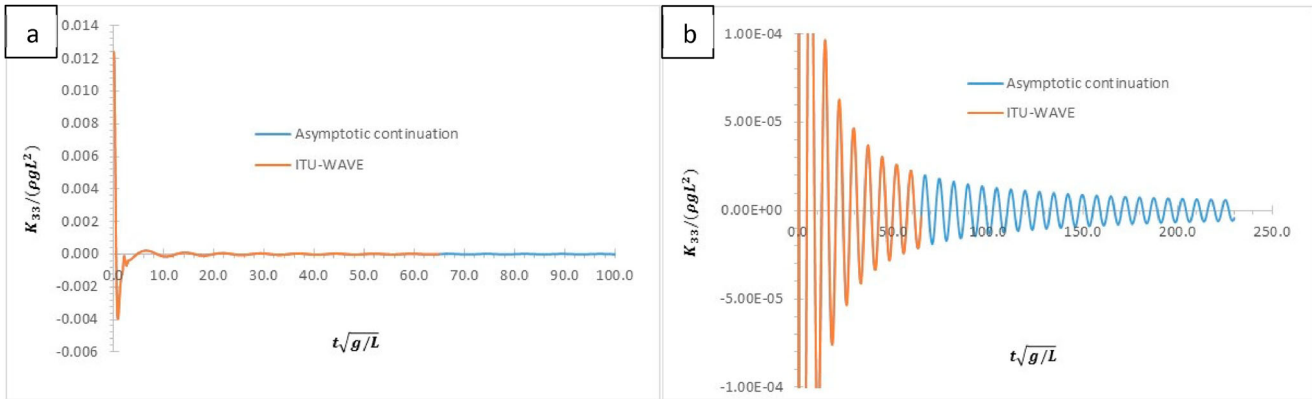


Figure 8. Potential method for Wigley hull form with Froude number $F_n = 0.3$ and nondimensional time step size $dt = 0.05$ (a) heave IRF (b) expanded view of heave IRF. (This figure is available in colour online.)

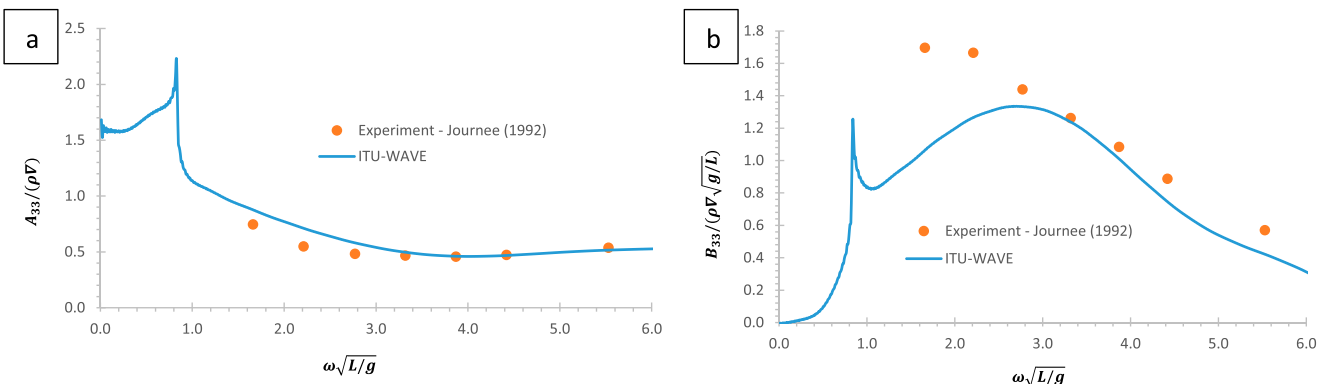


Figure 9. Potential method for Wigley hull form with Froude number $F_n = 0.3$ and nondimensional time step size $dt = 0.05$ (a) heave added-mass coefficients (b) damping coefficients. (This figure is available in colour online.)

The time dependent diffraction IRF $K_{jD}(t)$ in Equation (19), which is the IRF in j -th direction, are the functions of Froude-Krylov IRF $K_{jI}(t)$ due to incident waves $\zeta(t)$ with heading angle β and scattering IRF $K_{jS}(t)$ due to the diffraction of the incident waves from the floating body surface. The diffraction force hydrodynamic parameters are predicted using a body-fixed coordinate system at which the impulsive incident wave elevation $\zeta(t)$ is described at the centre of the Cartesian coordinate system which is a time-invariant linear system. The impulsive incident waves result in the transient pressure $\hat{p}(P, t)$ on the floating system and transient scattering potential $\phi_S(P, t)$ which are used to predict the IRFs.

The analytically known incident wave potential $\varphi_I(P, t)$ in Equation (22) and arbitrary regular or irregular wave elevation $\zeta(t)$ at the centre of the coordinate system is used to predict the excitation of the floating systems (King 1987).

$$\varphi_I(P, t) = \frac{1}{\pi} \text{Re} \left\{ \int_{-\infty}^{\infty} d\omega_e \frac{ig}{\omega} e^{k(z-i\varpi)} e^{i\omega_e t} \right\} \quad (22)$$

where the position of the floating system in the wave direction on the free surface, wave number in infinite water depth, heading angle in the positive x -direction, linear system's absolute frequency, and encounter frequency are presented in Equation (22) with $\varpi = x \cos(\beta) + y \sin(\beta)$, $k = \omega^2/g$, β , ω , and ω_e , respectively. The forward speed in the positive x -direction of the floating body is given with U_0 . All frequencies for the motion

characteristics of the floating system are included with the incident wave potential $\varphi_I(P, t)$ in Equation (22), which is a uni-directional wave system.

Figure 10 shows the convergence of scattering (a) and diffraction (b) IRFs with a potential approximation at zero speed for a hemisphere. As compared to radiation IRFs, diffraction force IRFs components require a smaller number of panels for convergence. As can be observed from Figure 10, the convergence is achieved with even 144 panels.

Figure 11 shows the convergence of scattering (a) and diffraction (b) IRFs with source methods at zero speed for a hemisphere. As opposed to radiation IRFs for the source method, diffraction IRFs require much less panel number for convergence. The requirements of less panel number for convergence of scattering IRFs $K_{jS}(t)$ Equation (21) of diffraction problem compared to radiation IRFs $K_{jR}(t)$ Equation (9) can be attributed to the solution of the boundary integral equations of Equation (1) for the potential method and Equation (2) for the source method. In the case of radiation problem, the potential is decomposed into impulsive ($\psi_{1k}(P)$ and $\psi_{2k}(P)$) part and transient part ($\chi_k(P, t)$). The solution of transient potential $\chi_k(P, t)$ includes the numerical prediction of the time independent impulsive potentials $\psi_{1k}(P)$ and $\psi_{2k}(P)$, in addition to analytical integration of the Rankine parts (e.g. $1/r$, $1/r'$) and numerical integration of the memory part of the transient wave Green function $\tilde{G}(P, Q, t - \tau)$ Equation (4). On the other hand, in the case of diffraction problem, although the same integral equations are used, scattering potential $\phi_S(P, t)$ is not decomposed into different potentials and the body boundary condition is

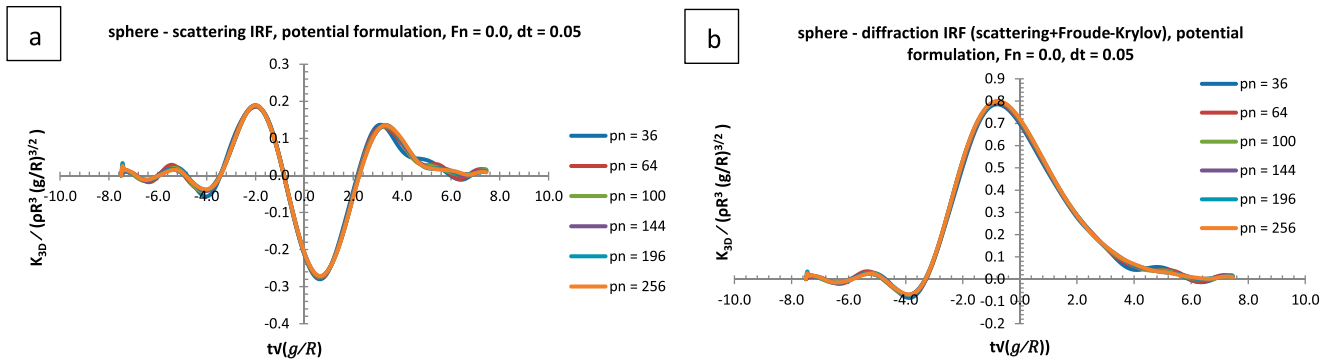


Figure 10. Potential method, convergence test in a range of panel numbers, Froude numbers $F_n = 0.0$ and nondimensional time step size 0.05 for hemisphere (a) heave scattering IRF (b) diffraction (scattering + Froude-Krylov) IRF. (This figure is available in colour online.)

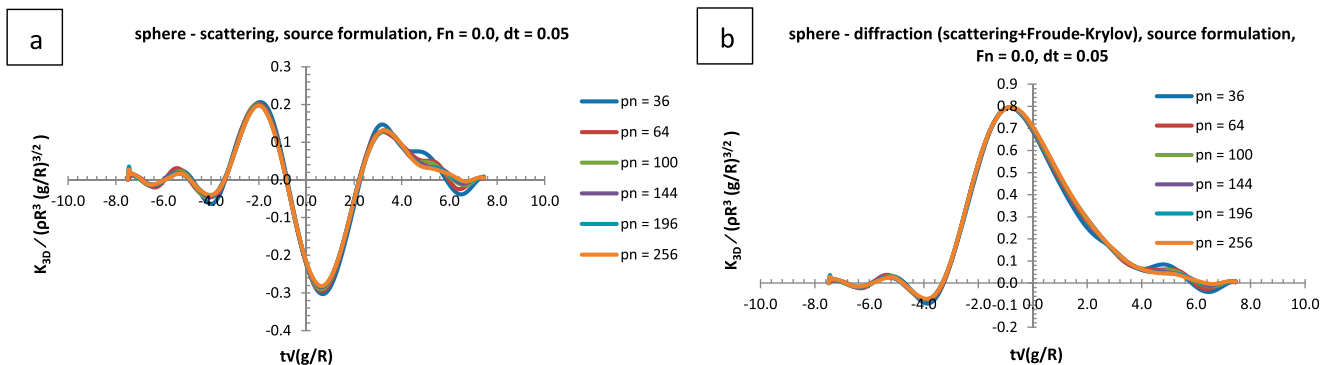


Figure 11. Source method, convergence test in a range of panel numbers, Froude numbers $F_n = 0.0$ and nondimensional time step size 0.05 for a hemisphere (a) heave scattering IRF (b) diffraction (scattering + Froude-Krylov) IRF. (This figure is available in colour online.)

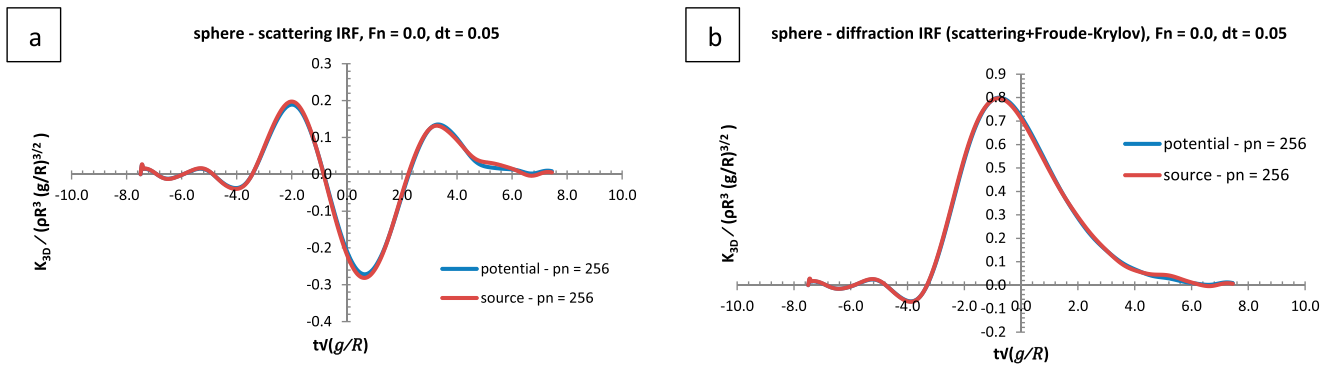


Figure 12. Comparison of potential and source methods for heave IRFs of a hemisphere at Froude number $F_n = 0.0$ and nondimensional time step size 0.05 (a) scattering (b) diffraction (scattering + Froude-Krylov). (This figure is available in colour online.)

predicted analytically (King 1987). As observed in Figure 11, the convergence with the source method is achieved with $pn = 144$ panels opposite to panel number $pn = 1444$, in the case of radiation IRFs.

Figure 12 shows the comparison of heave scattering (a) and diffraction (b) IRFs with source and potential methods at zero forward speed for a hemisphere. As can be seen in Figure 12, both potential and source IRFs are converged at the same panel numbers as opposed to radiation IRFs.

4. Application of the potential method to multi-hull floating systems

As the potential method achieves convergence much faster than the source method in the case of the prediction of radiation IRFs, the potential method will be used for the approximations of twin-hull high-speed craft's hydrodynamic and motion parameters, in this section. The twin-hull floating structures experience significant hydrodynamic interactions if they are in sufficiently closer proximity. When they are disturbed at their mean positions, twin-hull start to oscillate and generate waves. Some of these generated waves are radiated back to infinity while others interact with floating bodies in the twin-hull system which result in the diffraction of the waves by bodies. The existence and interaction of waves with floating bodies significantly change the motion behaviour, hydrodynamic forces, seakeeping, and manoeuvring performances of the multi-hull floating systems.

The multi-hull interactions have many applications in the industry including towing of a ship, offshore platforms with multiple columns, multi-hull ships and catamarans, wave energy converters in an array system, replenishment of two ships and transfer of the

cargo with multi-hull systems in a seaway. The wave interactions in the gap of multi-hull systems due to standing waves result in the resonance at which the complete transmission or complete reflection of the incident waves can happen (Newman 1974; Evans 1975).

4.1. Twin-hull high-speed craft with potential method prediction

The present in-house ITU-WAVE computational results including added-mass coefficient, damping coefficient, diffraction force amplitude, diffraction force phase angle at heading angle $\beta = 180^\circ$ and Response Amplitude Ratio (RAO) in heave and pitch modes using 196 panels on a single-hull are validated with the experimental results of DUT (Delft University of Technology) twin-hull high-speed craft (Van't Veer 1998). The length L , length to draft ratio L/T , length to beam ratio L/B , separation distance ratio between hulls H/B , and Froude number F_n are given with $L = 3.0$ m, $L/T = 20$, $L/B = 12.5$, and $H/B = 2.917$, and $F_n = 0.75$, respectively. It may be noticed that a lesser number of panels ($pn = 196$) compared to hemisphere ($pn = 400$) for the potential method is required for the twin-hull form. When the hemisphere and twin-hull forms are compared, the hemisphere has full body form while the twin-hull has very slender hull form. It is known that the potential theory methods are much better suited and predict the hydrodynamic parameters of the slender hull forms accurately as slender bodies are streamlined hull forms.

4.1.1. Radiation force coefficients in frequency domain

Fourier transform is used to transfer the time domain results in Equation (5) to frequency domain results as presented in Equation

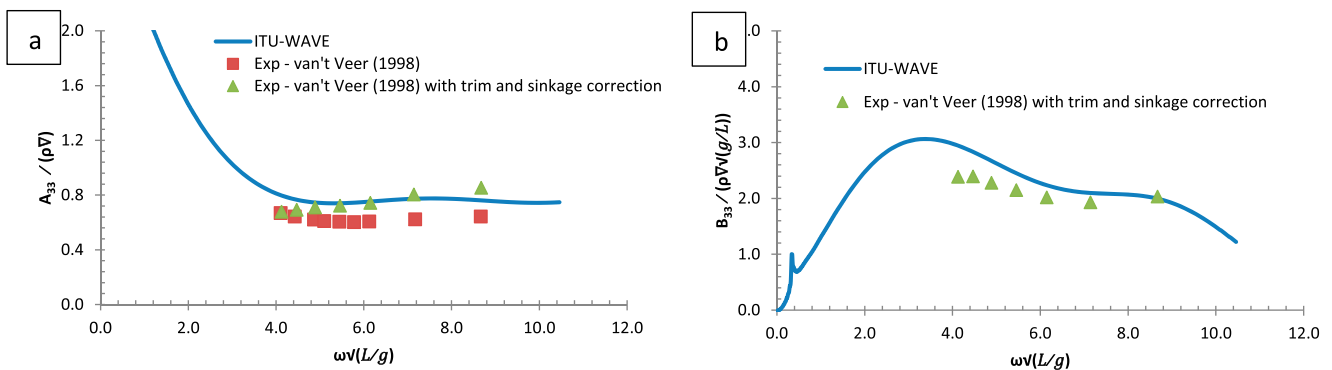


Figure 13. Twin-hull high-speed craft with $H/B = 2.917$, $L/T = 20$, $L/B = 12.5$ at Froude number $F_n = 0.75$, heave nondimensional (a) added-mass coefficient (b) damping coefficient. (This figure is available in colour online.)

(23) and Equation (24) in the case of a time harmonic motion.

$$A_{jk}(\omega) = a_{jk} - \frac{1}{\omega} \int_0^t d\tau K_{jk}(\tau) \sin(\omega\tau) - \frac{c_{jk}}{\omega^2} \quad (23)$$

$$B_{jk}(\omega) = b_{jk} + \int_0^t d\tau K_{jk}(\tau) \cos(\omega\tau) \quad (24)$$

where the added-mass and damping coefficient, which are the frequency dependent coefficients, are given with $A_{jk}(\omega)$ and $B_{jk}(\omega)$, respectively.

The present ITU-WAVE numerical results and experimental results (Van't Veer 1998), which include with and without trim and sinkage effects, are compared for validation purposes of the numerical results in Figure 13(a) and Figure 13(b). The present added-mass and damping coefficients results are obtained using the mean position of the twin-hull high-speed craft without considering the sinkage and trim moment effects. However, it can be seen in Figure 13 that the present ITU-WAVE numerical results of nondimensional heave added-mass coefficient Figure 13(a) and damping coefficient Figure 13(b) at very high Froude number $F_n = 0.75$ approximate the experimental results (Van't Veer 1998) satisfactorily.

The present ITU-WAVE numerical results of nondimensional cross-coupling heave-pitch and pitch-heave added-mass coefficients Figure 14(a) and damping coefficients Figure 14(b) are compared for validation purposes with experimental results (Van't Veer 1998) which also consider the effects of trim and sinkage corrections. As it can be seen in Figure 14, the numerical and experimental results are in good agreement. The experimental results of cross-

coupling added-mass coefficients show that there were no considerable effects of the trim and sinkage corrections. This is the reason that only experimental results without trim and sinkage corrections are presented in Figure 14(a).

The nondimensional pitch added-mass coefficients Figure 15(a) and damping coefficients Figure 15(b) of the present ITU-WAVE computational results are compared with experimental results (Van't Veer 1998). As in the heave and cross-coupling heave-pitch hydrodynamic coefficients, the present ITU-WAVE pitch added-mass and damping coefficients approximate the experimental results satisfactorily.

4.1.2. Diffraction force coefficients in frequency domain

As in radiation force, added-mass and damping coefficients in Equation (23) and Equation (24), the diffraction force amplitudes and phase angles in the frequency domain are obtained via Fourier transform of diffraction IRFs of Equation (19).

$$X_j(\omega_e) = \int_{-\infty}^{\infty} d\tau [K_{j1}(\tau) + K_{j5}(\tau)] e^{-i\omega\tau} \quad (25)$$

where the complex form of the diffraction force is given with $X_j(\omega_e)$. The frequency domain parameters of the diffraction force amplitudes and phase angles are the absolute values and arguments of Equation (25), respectively. The force amplitudes and phase angles of Froude-Krylov and scattering forces in the frequency domain are also obtained via Fourier transform of the time dependent IRFs of Equation (20) and Equation (21), respectively.

The frequency dependent heave and pitch diffraction force amplitudes and phase angles of the present ITU-WAVE

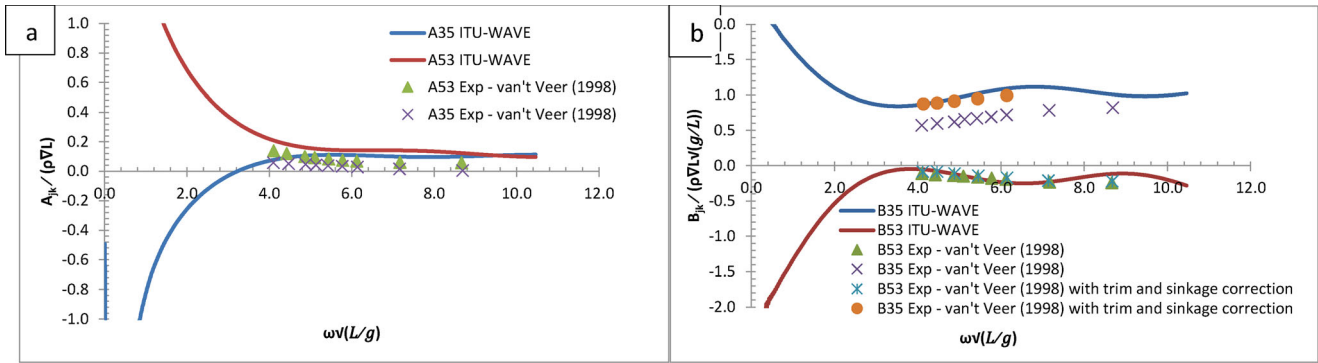


Figure 14. Twin-hull high-speed craft with $H/B = 2.917$, $L/T = 20$, $L/B = 12.5$ at Froude number $F_n = 0.75$, nondimensional cross-coupling heave-pitch and pitch-heave coefficients (a) added-mass coefficients (b) damping coefficients. (This figure is available in colour online.)

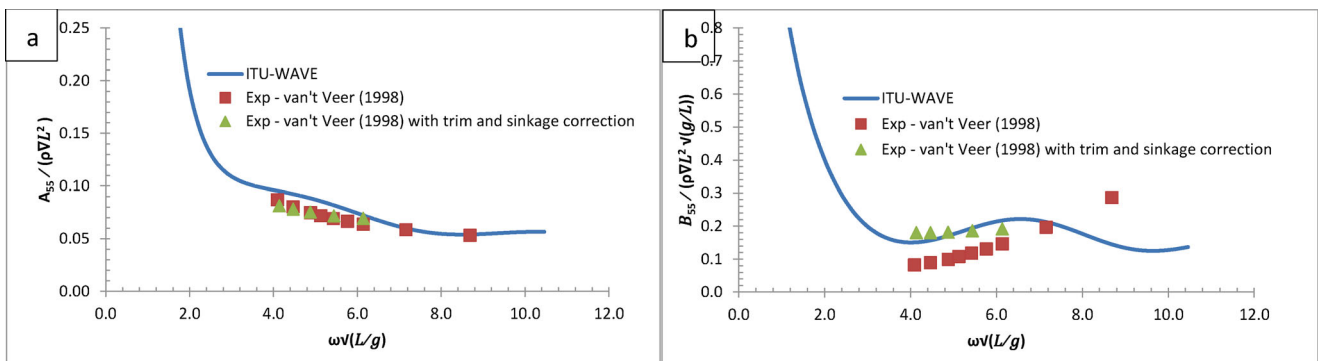


Figure 15. Twin-hull high-speed craft with $H/B = 2.917$, $L/T = 20$, $L/B = 12.5$ at Froude number $F_n = 0.75$, pitch nondimensional (a) added-mass coefficient (b) damping coefficient. (This figure is available in colour online.)

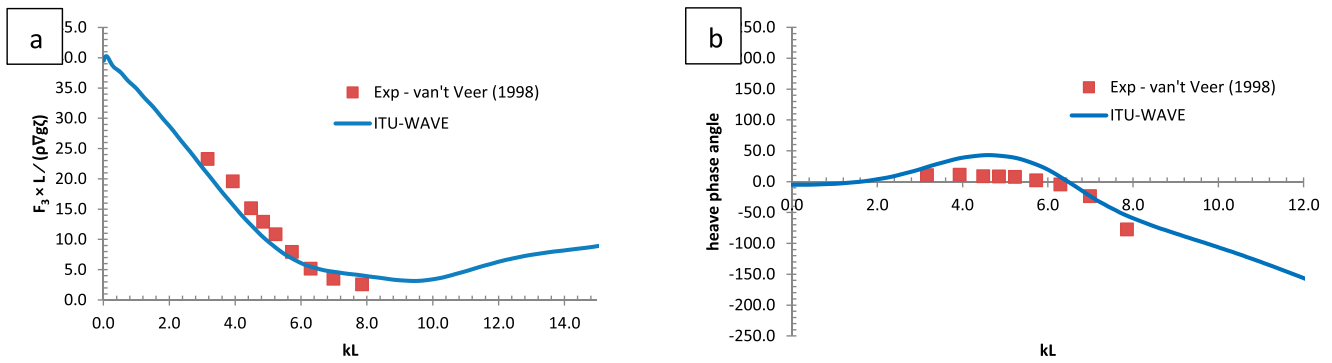


Figure 16. Twin-hull high-speed craft with $H/B = 2.917$, $L/T = 20$, $L/B = 12.5$ at heading angle $\beta = 180^\circ$ and Froude number $F_n = 0.75$, heave nondimensional (a) diffraction force amplitude (b) diffraction phase angle. (This figure is available in colour online.)

computational results in Figure 16(a,b), and Figure 17(a,b), respectively, which are the superpositions of scattering and Froude-Krylov forces, are validated with the experimental results (Van't Veer 1998) at Froude number $F_n = 0.75$ and heading angle $\beta = 180^\circ$. It can be observed from Figures 16 and 17 that the numerical and experimental results are in good agreement.

4.1.3. Response amplitude operators (RAOs) for the heave and pitch modes

The experimental results (Van't Veer 1998) of RAOs and phase angles in heave and pitch modes are used to compare and validate the present ITU-WAVE computational results at Froude number $F_n = 0.75$ and heading angle $\beta = 180^\circ$. The heave RAO in Figure 18 (a) and phase angle in Figure 18(b), and pitch RAO in Figure 19(a)

and phase angle in Figure 19(b) show satisfactory agreement with the experimental results (Van't Veer 1998).

The heave and pitch RAOs show different behaviours in a range of incident wave frequencies. The velocity and acceleration do not exist around the zero-frequency region so that this region is controlled by hydrostatic restoring forces. As the hydrostatic restoring force coefficients balance the force due to inertia around the resonance region, the damping forces dictate the resonance region where the incident wave frequency and natural frequency of the floating systems are equal. The floating system would not have enough time to respond to the incident wave at a higher frequency region so that this region is controlled by the mass of the floating systems.

As the DUT twin-hull has a transom stern, there would be flow separation due to immersion of the transom stern at a high Froude

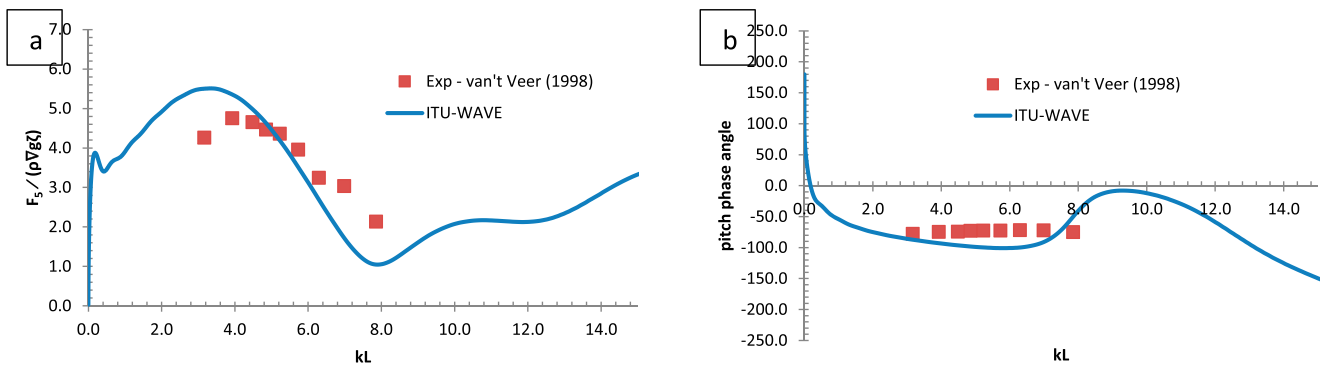


Figure 17. Twin-hull high-speed craft with $H/B = 2.917$, $L/T = 20$, $L/B = 12.5$ at heading angle $\beta = 180^\circ$ and Froude number $F_n = 0.75$, pitch nondimensional (a) diffraction force amplitude (b) diffraction phase angle. (This figure is available in colour online.)

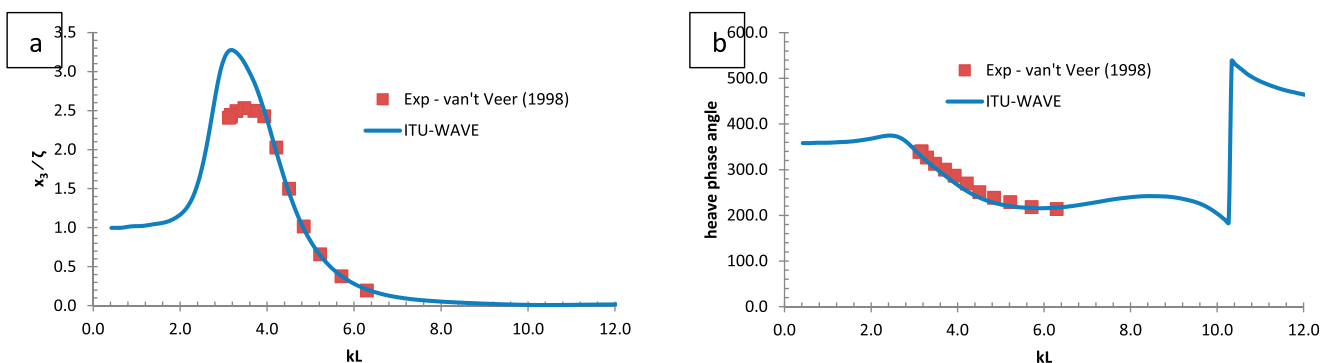


Figure 18. Twin-hull high-speed craft with $H/B = 2.917$, $L/T = 20$, $L/B = 12.5$ at heading angle $\beta = 180^\circ$ and Froude number $F_n = 0.75$, heave nondimensional (a) force amplitude (RAO) (b) phase angle. (This figure is available in colour online.)

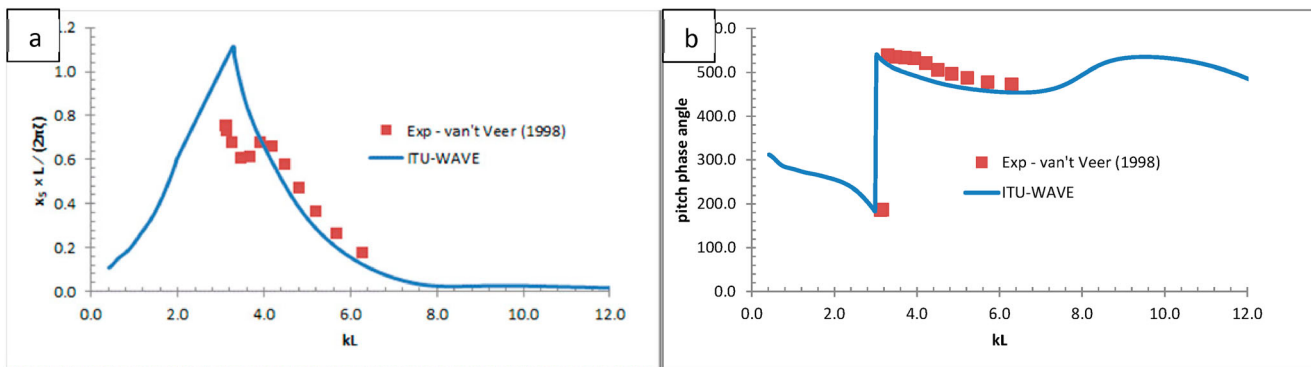


Figure 19. Twin-hull high-speed craft with $H/B = 2.917$, $L/T = 20$, $L/B = 12.5$ at heading angle $\beta = 180^\circ$ and Froude number $F_n = 0.75$, pitch nondimensional (a) force amplitude (RAO) (b) phase angle. (This figure is available in colour online.)

number $F_n = 0.75$. The flow separation influences the viscous effects which would affect the response amplitude at the resonance frequency region as can be observed in Figures 18 and 19. However, the viscous damping is usually limited for slender vessels advancing at high speed in head sea waves while an important damping effect is the hull-lift damping for which dry transom stern is important (Faltinsen 2005). Owing to the increase in viscosity and hull-lift damping, the damping of the floating system would increase which result in the reduction of the motion amplitude. It is expected that the potential theory based numerical methods overpredict the motion amplitudes as the potential theory ignore the viscous effects and hull-lift damping. As the ITU-WAVE numerical code depends on the three-dimensional potential formulation for arbitrary multi-hull bodies, the overprediction of wave amplitudes can be observed clearly for heave and pitch modes in Figures 18 and 19 at resonance region, while the phase angles for both heave and pitch modes are in better agreement with the experimental results. The ITU-WAVE numerical results also show a small shift against the experimental results in motion amplitudes towards higher frequencies in the pitch mode as in Figure 19.

5. Conclusions

The application of the in-house three-dimensional transient wave-body interaction computational tool ITU-WAVE with the boundary integral equation method and Neumann-Kelvin linearization is presented for the time domain prediction of different hydrodynamic parameters including multi-hull interactions, RAOs and first-order unsteady hydrodynamic forces (e.g. the radiation and diffraction forces of isolated and twin-hull floating systems in time and frequency domains).

The numerical comparisons of the potential and source methods are presented depending on the convergence of numerical results in terms of the panel numbers against the analytical result in the case of the hemisphere. Numerical experiences show that in the case of radiation force IRFs the potential method achieves the numerical convergence much faster than the source method in terms of panel numbers, while in the case of diffraction force IRFs, both potential and source methods achieve the convergence approximately with the same number of panels.

Numerical results related to radiation and diffraction (including Froude-Krylov and scattering) forces in the frequency domain are obtained by Fourier transform of the transient radiation and diffraction time domain IRFs, respectively. The ITU-WAVE numerical results for the heave and pitch RAOs, added-mass and damping

coefficients, diffraction force amplitudes and phase angles show a satisfactory agreement with analytical and experimental results.

Disclosure statement

No potential conflict of interest was reported by the author(s).

References

- Adachi H, Ohmatsu S. 1979. On the influence of irregular frequencies in the integral equation solution to the time-dependent free surface problems. *J Soc Naval Architect Japan*. 146:127–135.
- Baker GR, Meiron DI, Orszag SA. 1982. A generalized vortex methods for free surface flow problem. *J Fluid Mech*. 123:477–501.
- Beck RF. 1999. Fully nonlinear water wave computations using a desingularized Euler-Lagrange time domain approach. *Nonlinear Water Wave Interaction*, p. 1–57.
- Beck RF, Liapis S. 1987. Transient motions of floating bodies at zero-forward speed. *J Ship Res*. 31(3):164–176.
- Beck RF, Magee AR. 1991. Time domain analysis for predicting ship motions. *Proceedings of the IUTAM Symposium on the Dynamics of Marine Vehicles and Structures in Waves*, Brunel University, p. 49–64.
- Bingham HB. 1994. *Simulating ship motions in the time domain* [PhD thesis]. MIT, USA
- Cummins WE. 1962. The impulse response function and ship motions. *Shiffstechnik*. 9:101–109.
- Dagan T, Miloh G. 1980. Flow past oscillating bodies at resonance frequency. *Proceedings of 13th Symposium on Naval Hydrodynamics*, 355–373.
- Danmeier DG. 1999. *A higher-order panel method for large-amplitude simulations of bodies in waves* [PhD Thesis]. MIT.
- Evans DV. 1975. A note on the total reflection or transmission of surface waves in the presence of parallel obstacles. *J Fluid Mech*. 67:465–472.
- Faltinsen OM. 1977. Numerical solution of transient nonlinear free surface motion outside or inside moving bodies. *Proceedings of the 2nd International Conference on Numerical Ship Hydrodynamics*, Berkeley, California, CA, p. 347–357.
- Faltinsen OM. 2005. *Hydrodynamics of high-speed marine vehicles*. Cambridge: Cambridge University Press.
- Ferrant P. 1990. A coupled time and frequency approach for nonlinear wave radiation. *Proceedings of the 18th Symposium on Naval Hydrodynamics*, Ann Arbor, Michigan, p. 67–84.
- Finkelstein AB. 1957. The initial-value problem for transient water waves. *Commun Pure Appl Math*. 10:511–522.
- Hess JL, Smith AMO. 1964. Calculation of non-lifting potential flow about arbitrary three-dimensional bodies. *J Ship Res*. 8:22–44.
- Hulme A. 1982. The wave forces acting on a floating hemisphere undergoing forced periodic oscillations. *J Fluid Mech*. 121:443–463.
- Inoue Y, Kamruzzaman M. 2008. Analysis of hydrodynamic characteristics for arbitrary multihull ships advancing in waves. *J Mar Sci Technol*. 13:231–243.
- Journee JMJ. 1992. *Experiment and calculations on four Wigley hullforms*. Report No. 909, Delft University of Technology Ship Hydrodynamics Laboratory.
- Kara F. 2000. *Time domain hydrodynamics and hydroelastics analysis of floating bodies with forward speed* [PhD thesis]. University of Strathclyde, UK.

- Kara F. 2010. Time domain prediction of power absorption from ocean waves with latching control. *Renew Ener.* 35:423–434.
- Kara F. 2011. Time domain prediction of added-resistance of ships. *J Ship Res.* 55(3):163–184.
- Kara F. 2015. Time domain prediction of hydroelasticity of floating bodies. *Appl Ocean Res.* 51:1–13.
- Kara F. 2016a. Time domain prediction of power absorption from ocean waves with wave energy converter arrays. *Renew Ener.* 92:30–46.
- Kara F. 2016b. Time domain prediction of seakeeping behaviour of catamarans. *Inter Shipbuild Progress.* 62(3–4):161–187.
- Kara F. 2016c. Point absorber wave energy converter in regular and irregular waves with time domain analysis. *Inter J Marine Sci Ocean Technol.* 3(7):74–85.
- Kara F. 2017. Control of wave energy converters for maximum power absorptions with time domain analysis. *J Fund Renew Ener Appl.* 7(1):1–8.
- Kara F. 2020a. A control strategy to improve the efficiency of point absorber wave energy converters in complex sea environments. *J Marine Sci Res Ocean.* 3(2):43–52.
- Kara F. 2020b. Multibody interactions of floating bodies with time domain predictions. *J Water Port Coastal Ocean Eng.* 146.
- Kara F. 2021a. Hydroelastic behaviour and analysis of marine structures. *J Sustain Marine Struct.* 2(1):14–24.
- Kara F. 2021b. Applications of time domain methods for marine hydrodynamic and hydroelasticity analyses of floating systems. *Ships Offsh Struct.* <https://doi.org/10.1080/17445302.2021.1937798>.
- Kara F. 2021c. Hydrodynamic performances of wave energy converters arrays in front of a vertical wall. *Ocean Eng.* 235:109459.
- Kara F, Tang C, Vassalos D. 2007. Time domain three dimensional fully nonlinear computations of steady body-wave interaction problem. *Ocean Eng.* 34(5):776–789.
- Kim CH, Chou FS, Tien D. 1980. Motion and hydrodynamic loads of a ship advancing in oblique waves. *Trans Soc Naval Archi Marine Eng.* 88:225–256.
- King B. 1987. Time domain analysis of wave exciting forces on ships and bodies [PhD Thesis]. University of Michigan.
- Korvin-Kroukovsky BV, Jacobs WR. 1957. Pitching and heaving motions of a ship in regular waves. *Trans Soc Naval Archi Marine Eng.* 65:590–632.
- Kring D, Sclavounos PD. 1991. A new method for analyzing the seakeeping of multi-hull ships. *Proceedings of 1st International Conference on Fast Sea Transportation, Trondheim, Norway,* p. 429–444.
- Liapis S. 1986. Time domain analysis of ship motions [PhD Thesis]. University of Michigan.
- Liapis S, Beck RF. 1985. Seakeeping computations using time domain analysis. *Proceedings of the 4th International Symposium on Numerical Hydrodynamics, Washington, DC,* p. 34–54.
- Lin WC, Yue DKP. 1990. Numerical solutions for large amplitude ship motions in the time domain. *Proceedings of the 18th Symposium on Naval Hydrodynamics, Ann Arbor, Michigan,* p. 41–66.
- Longuet-Higgins MS, Cokelet ED. 1976. The deformation of steep surface waves on water- a numerical method of computation. *Proc Royal Soc London, Series A.* 350:1–26.
- Nakos D, Sclavounos PD. 1990. Ship motions by a three dimensional Rankine panel method. *Proceedings of the 18th Symposium on Naval Hydrodynamics, Ann Arbor, Michigan, USA,* p. 21–41.
- Newman JN. 1974. Interactions of water waves with two closely spaced vertical obstacles. *J Fluid Mech.* 66:97–106.
- Newman JN. 1985. Transient axisymmetric motion of a floating cylinder. *J Fluid Mech.* 157:17–33.
- Newman JN. 1992. The approximation of free-surface Green functions. *Wave Asymptotic.* 1:107–135.
- Ogilvie TF. 1964. Recent progress toward the understanding and prediction of ship motions. *Proceedings of 5th Symposium on Naval Hydrodynamics, Office of Naval Research, Washington, DC, USA,* p. 3–128.
- Ogilvie TF, Tuck EO. 1969. A rational strip theory for ship motions, Part 1. Report No. 013, The Department of Naval Architecture and Marine Engineering, The University of Michigan, Ann Arbor, Michigan.
- Salvensen N, Tuck EO, Faltinsen O. 1970. Ship motions and sea loads. *Trans Soc Naval Archi Marine Eng.* 78:250–287.
- Van't Veer AP. 1998. Experimental results of motions, hydrodynamic coefficients and wave loads on the 372 catamaran model. Report, No.1129, Delft University of Technology, The Netherlands.
- Vinje T, Brevig P. 1981. Nonlinear ship motions. *Proceedings of the 3rd International Symposium on Numerical Hydrodynamics,* p. 257–268.
- Wehausen JV, Laitone EV. 1960. Surface waves. *Handbuch der Physik.* 9:446–778.
- Xiang X, Faltinsen OM. 2011. Time domain simulation of two interacting ships advancing parallel in waves. *Proceedings of the ASME 30th International Conference on Ocean, Offshore and Arctic Engineering, Rotherdam, The Netherlands.*
- Yuan Z-M, Incecik A, Alexander D. 2014. Verification of a new radiation condition for two ships advancing in waves. *Appl Ocean Res.* 48:186–201.
- Zou L, Zou Z-J, Liu Y. 2019. CFD-based predictions of hydrodynamic forces in ship-tug boat interactions. *Ships Offsh Struct.* 14:300–310.